JOURNAL OF PROPULSION AND POWER
Vol. 17, No. 4, July–August 2001

Computation of Compressible Flows Through a Chemical Laser Device with Crossflow Injection

James H. Miller,* Joe S. Shang,† Robert F. Tomaro,‡ and William Z. Strang§
U.S. Air Force Research Laboratory, Wright–Patterson Air Force Base, Dayton, Ohio 45433

The Air Force Research Laboratory has an ongoing effort to develop an accurate and efficient computational tool to support the development of advanced chemical oxygen/iodine laser (COIL) devices. In this study, a series of computational simulations have been performed to provide a better understanding of fluid dynamic phenomena within geometries associated with COIL flowfields. The parallel, implicit unstructured Navier–Stokes code Cobalt$_{60}$ was used to compute laminar, turbulent, and unsteady flows of helium within the research assessment and device improvement chemical laser (RADICL) nozzle. Computational results showing details of the jet mixing interaction and topological structure are presented. The laminar and turbulent results obtained with Cobalt$_{60}$ are in excellent agreement with measured mass flow rates and surface pressure data obtained from recent cold-flow tests performed with the RADICL device. Insufficient experimental measurement prevents the determination of whether or not transition occurs within the injector region. The laminar time-accurate results indicate small-scale unsteadiness in the frequency range of 200 kHz downstream of the nozzle throat.

Nomenclature

A	=	cross-sectional area
A, B, C, D	=	grid labels (D is finest grid)
a	=	speed of sound
a, b, c	=	viscous terms in energy equation [see Eq. (2)]
c_x^{t1}, c_x^{t2}	=	x-direction convection terms for turbulence
c_y^{t1}, c_y^{t2}	=	y-direction convection terms for turbulence
c_z^{t1}, c_z^{t2}	=	z-direction convection terms for turbulence
D	=	diameter of injector
$\boldsymbol{D}$	=	volumetric source term vector
D^{t1}, D^{t2}	=	source terms for turbulence closure equations
$\mathrm{d}S$	=	differential surface
$\mathrm{d}V$	=	differential volume
E_t	=	total energy, $\rho[e + \frac{1}{2}(u^2 + v^2 + w^2)]$
$\boldsymbol{f}, \boldsymbol{g}, \boldsymbol{h}$	=	x, y, and z components of inviscid fluxes
$\hat{i}, \hat{j}, \hat{k}$	=	Cartesian unit vectors
k	=	thermal conductivity, turbulence kinetic energy
M	=	Mach number
M	=	molecular weight
n	=	normal distance from wall
$\dot{n}$	=	molar flow rate
$\hat{n}$	=	unit normal vector
p	=	pressure
$\boldsymbol{Q}$	=	vector of conserved variables
Re	=	Reynolds number
$\boldsymbol{r}, \boldsymbol{s}, \boldsymbol{t}$	=	x, y, and z components of viscous fluxes
S	=	surface of control volume
T	=	temperature
t	=	time
u, v, w	=	Cartesian components of velocity
V	=	volume
$\boldsymbol{V}$	=	velocity vector
v_x^{t1}, v_x^{t2}	=	x-direction diffusion terms for turbulence
v_y^{t1}, v_y^{t2}	=	y-direction diffusion terms for turbulence
v_z^{t1}, v_z^{t2}	=	z-direction diffusion terms for turbulence
x, y, z	=	Cartesian coordinate directions
γ	=	ratio of specific heats
Δ	=	discrete change in variable
θ	=	implicit–explicit weighting factor
μ	=	molecular viscosity
μ_t	=	turbulent viscosity
Π	=	penetration parameter
τ, $\bar{\bar{\tau}}$	=	viscous stress
ϕ_{t1}, ϕ_{t2}	=	scalar turbulence quantities
ω	=	rate of dissipation per unit turbulence kinetic energy

Subscripts

g	=	ghost cell
i	=	interior cell
l	=	local conditions at point of injection
o	=	measured subsonic conditions
p	=	primary flow
s	=	secondary (injector) flow
t	=	total, turbulent
w	=	wall
x, y, z	=	vector or partial derivative components
xx, xy, xz yy, yz, zz	=	viscous stress components
1	=	first point above wall

Superscripts

t	=	tangential component
$t1, t2$	=	first and second turbulence closure equation
τ	=	viscous stress
$+$	=	normalized with respect to wall shear stress

Presented as Paper 2000-2575 at the AIAA 31st Plasmadynamics and Lasers Conference, Denver, CO, 19–22 June 2000; received 9 August 2000; revision received 5 February 2001; accepted for publication 5 February 2001.

*Visiting Scientist, VAAC, Ohio Aerospace Institute; currently Ohio Aerospace Institute Senior Research Associate, Air Vehicles Directorate. Senior Member AIAA.

†Leader, Computational Sciences Center of Excellence, Air Vehicles Directorate. Fellow AIAA.

‡Aerospace Engineer, Air Vehicles Directorate; currently Research Engineer, Cobalt Solutions, LLC, Dayton, OH 45459.

§Aerospace Engineer, Air Vehicles Directorate; currently Research Engineer, Cobalt Solutions, LLC, Dayton, OH 45459.

I. Introduction

THE chemical oxygen/iodine laser (COIL) has been an important research topic in the U.S. Air Force (USAF) since the first successful demonstration in 1977.[1] The COIL is unique among chemical lasers because it is the only high-power chemical laser to utilize electronic transition rather than vibrational transition.[2] The

current USAF airborne laser program has focused on military applications of COIL technology,[3] although commercial applications are also receiving significant attention.[4–6]

The supersonic COIL was first demonstrated at the USAF Weapons Lab.[7] The complexity of a supersonic COIL is well known and contains many challenges to detailed modeling using computational fluid dynamics (CFD). Within the flowfield of the COIL there is multiphase flow, molecular diffusion, chemical nonequilibrium, thermal nonequilibrium, and stimulated emission of photons. To model the complete COIL lasing interaction, a three-dimensional formulation of the fluid dynamics, species continuity, and radiation transport equations is necessary.

There have been many approaches to simulation of COIL devices, not only in the U.S. but other nations as well. Examples are Israel,[8,9] Russia,[10] China,[11] and European countries.[12,13] Researchers in Japan have demonstrated much experimental and computational progress[14–17] as well. Only a brief overview of work in the U.S. is given here. Much of the early modeling of COIL devices was done by Crowell.[18,19] A complete end-to-end model, including the rotating disk oxygen generator and the nozzle/cavity/resonator system, was presented by Crowell and Plummer in 1993.[20] Buggeln et al.[21] coupled the radiation transport with the three-dimensional Navier–Stokes equations and modeled the region from the injectors to the cavity where the power extraction occurs. Lampson et al.[22,23] investigated laser beam quality issues with the MINT and OCELOT codes. Yang et al.[24] have developed an efficient approximate method to calculate COIL performance quantities including iodine dissociation, excited-state pumping, quenching, and optical extraction from a stable resonator. Madden and Solomon[25] and Madden et al.[26] have modeled the three-dimensional chemically reacting flowfield of the COIL under nonlasing conditions, and, more recently, Madden et al. have done so with theoretical power extraction.[27]

Although these studies have shown reasonable comparisons with measured gain, power, and dissociation data,[8–27] they have provided incomplete insight into some of the fluid dynamic effects within COIL flowfields. This is due in part to two key reasons. First, the computational resources required to obtain detailed resolution of COIL flowfields are formidable. Second, the experimental data used to validate existing CFD models are incomplete for verifying important fluid dynamic assumptions, such as laminar or turbulent flow, and the unsteadiness within the COIL.

In this study, the parallel, implicit unstructured flow solver Cobalt$_{60}$[28] is used in an attempt to determine the effects on computed results obtained from laminar or turbulent assumptions. The effects of Reynolds number for the same jet-penetration conditions are also investigated. In addition, dominant unsteady frequencies are determined by utilizing time-accurate methods of integration. The current study thus aims to provide a better understanding of the fluid dynamics within the research assessment and device improvement chemical laser (RADICL) nozzle and assess the impact of modeling assumptions used in modeling nonreacting flows within the RADICL device. To support the current effort, two cold-flow experiments were performed by the Directed Energy Directorate at Kirtland Air Force Base, New Mexico where helium was used for the primary and secondary flows through the RADICL nozzle. The present numerical results are in excellent agreement with the measured mass flow rates and wall pressures when both laminar and turbulent modeling assumptions are used.

II. Governing Equations

The governing equations consist of the Navier–Stokes equations and turbulence closure models that are solved in finite volume form and that can be written as follows:

$$\frac{\partial}{\partial t}\iiint_V \boldsymbol{Q}\,\mathrm{d}V + \iint_S (\boldsymbol{f}\hat{i} + \boldsymbol{g}\hat{j} + \boldsymbol{h}\hat{k})\cdot\hat{n}\,\mathrm{d}S = \iint_S (\boldsymbol{r}\hat{i} + \boldsymbol{s}\hat{j} + \boldsymbol{t}\hat{k})\cdot\hat{n}\,\mathrm{d}S + \iiint_V \boldsymbol{D}\,\mathrm{d}V \tag{1}$$

where

$$\boldsymbol{Q} = \begin{bmatrix} \rho \\ \rho u \\ \rho v \\ \rho w \\ E_t \\ \phi^{t1} \\ \phi^{t2} \end{bmatrix}, \quad \boldsymbol{f} = \begin{bmatrix} \rho u \\ \rho u^2 + p \\ \rho uv \\ \rho uw \\ (E_t + p)u \\ c_x^{t1} \\ c_x^{t2} \end{bmatrix}, \quad \boldsymbol{g} = \begin{bmatrix} \rho v \\ \rho uv \\ \rho v^2 + p \\ \rho vw \\ (E_t + p)v \\ c_y^{t1} \\ c_y^{t2} \end{bmatrix}$$

$$\boldsymbol{h} = \begin{bmatrix} \rho u \\ \rho u^2 + p \\ \rho uv \\ \rho uw \\ (E_t + p)u \\ c_z^{t1} \\ c_z^{t2} \end{bmatrix}, \quad \boldsymbol{r} = \begin{bmatrix} 0 \\ \tau_{xx} \\ \tau_{xy} \\ \tau_{xz} \\ a \\ v_x^{t1} \\ v_x^{t2} \end{bmatrix}, \quad \boldsymbol{s} = \begin{bmatrix} 0 \\ \tau_{xy} \\ \tau_{yy} \\ \tau_{yz} \\ b \\ v_y^{t1} \\ v_y^{t2} \end{bmatrix}$$

$$\boldsymbol{t} = \begin{bmatrix} 0 \\ \tau_{xz} \\ \tau_{yz} \\ \tau_{zz} \\ c \\ v_z^{t1} \\ v_z^{t2} \end{bmatrix}, \quad \boldsymbol{D} = \begin{bmatrix} 0 \\ 0 \\ 0 \\ 0 \\ 0 \\ D^{t1} \\ D^{t2} \end{bmatrix} \tag{2}$$

In these equations, $a = u\tau_{xx} + v\tau_{xy} + w\tau_{xz} + kT_x$, $b = u\tau_{xy} + v\tau_{yy} + w\tau_{yz} + kT_y$, and $c = u\tau_{xz} + v\tau_{yz} + w\tau_{zz} + kT_z$. The first five rows of this matrix equation are the conservation equations for mass; x, y, and z momentum; and energy, respectively. The last two rows are finite volume formulations of turbulence transport equations. More details on the turbulence modeling can be found in Refs. 29 and 30.

III. Algorithm

The numerical algorithm implemented in Cobalt$_{60}$ has been described in other references.[28,31,32] Only a brief description of the method will be given here. The Cobalt$_{60}$ code is a parallel, implicit unstructured flow solver. It is based on a cell-centered finite volume method that utilizes the exact Riemann solver of Gottlieb and Groth.[33] Second-order spatial accuracy is achieved by the least-squares total variation diminishing (TVD) method of Strang et al.[28] Viscous fluxes are formulated to satisfy the discrete maximum principle,[34] guarantee conservation, and yield a linearity preserving discretization.[28]

The time integration method is that of Tomaro et al.[32] with modifications by Strang et al.[28] Fully implicit time integration is used with first-order or second-order accuracy. Temporal damping is utilized following Jameson and Turkel[35] and Yoon and Kwak.[36] Newton subiterations can be used for unsteady flows that require very large time steps.[32] Because of the expensive computation of the Jacobians for the exact Riemann solver, the inviscid flux Jacobians are replaced with the Jacobians of van Leer's split fluxes (see Ref. 37). Experience has shown that convergence to steady state is fastest with moderate damping and very large time steps [Courant–Friedrichs–Lewy (CFL) number $= 10^6$]. For time-accurate calculations, the time step required for acceptable accuracy is usually small enough that temporal damping does not affect the temporal accuracy.[28]

Grismer et al.[31] have reported the development of the parallel version of Cobalt$_{60}$. In the parallel approach, the computational domain is broken up into subdomains where each processor solves the governing equations on its subdomain. Information is passed between processors using the message passing interface (MPI) library routines. To improve the convergence properties of the iterative method, the ordering scheme of Cuthill–McKee (see Ref. 38)

is used to maximize the number of neighboring cells that have been updated prior to the current cell. In addition, the domain decomposition is performed with the METIS system of Karypis and Kumar.[39] This approach to domain decomposition has demonstrated rapid generation of nearly equally balanced subdomains with minimum interfaces between zones.

IV. Grid Generation

The geometry used for the simulations is shown in Figs. 1 and 2. The complete RADICL device has 230 large injectors and 460 small injectors. The width (perpendicular to page in Fig. 1) of the entire nozzle is nominally 25.4 cm with 115 large injectors and 230 small injectors on the upper and lower walls, respectively. The computational domain in this study utilizes the so-called unit cell approximation based on geometric symmetry of the RADICL nozzle (see Fig. 2). In this approximation, $\frac{1}{460}$ of the entire nozzle flow is simulated where the computational domain utilizes three symmetry planes. These symmetry planes include the nozzle centerline, the centerline passing through the large injector, and the symmetry line bisecting the distance between the small injectors.

In this study, structured grids were developed using GRIDGEN.[40] The structured grids in this study utilized a multiblock approach. Four grids were used to verify grid independence and each grid consisted of 13 blocks. The dimensions of the grids within the nozzle (not including the exterior injector blocks) are given in Table 1.

A top view of grid D near the injector region is shown in Fig. 3. The blocks within the injectors had 33 points in the y direction. Within the large injector, the core block and the large boundary sector block had dimensions of 25×13, and the two small boundary sector blocks had dimensions of 13×13. Within the small injector, the core block had dimensions of 17×17, and the four boundary sector blocks had dimensions of 9×17. These injector grids were found to be adequate to resolve the boundary layers within each injector.

Table 1 Multiblock grid dimensions

Grid name	I	J	K
A	478	61	49
B	612	61	49
C	612	93	49
D	612	121	49

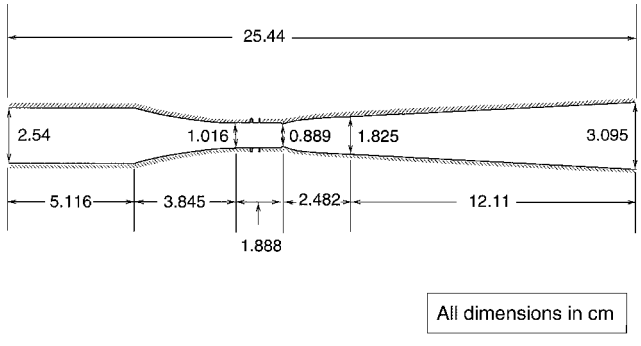

Fig. 1 RADICL nozzle geometry, side view.

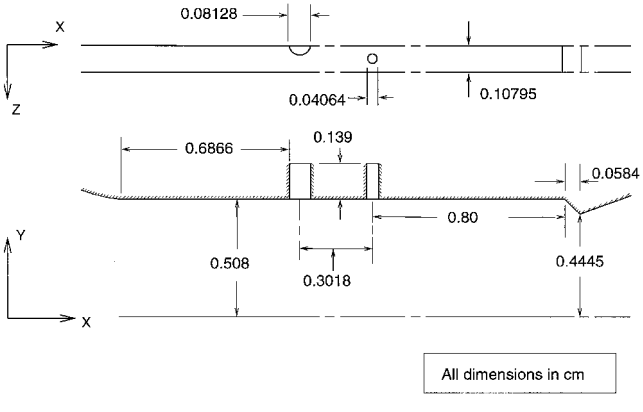

Fig. 2 RADICL nozzle geometry, top and side views of simulated injector region.

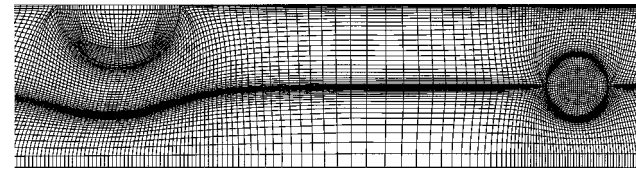

Fig. 3 Grid in injector region.

The largest multiblock grid (D) contained approximately 3.8 million cells, 4.3 million points, and 11.8 million faces. To resolve the boundary layer near the throat region, the normal spacing at the wall was $\Delta n = 3.3 \times 10^{-4}$ cm. In the injectors, the spacing normal to the injector wall was $\Delta n = 6.0 \times 10^{-4}$ cm. More details on the grids used in this study are given in Ref. 41.

V. Boundary Conditions

No-slip boundary conditions are used for the solid walls, and the wall temperatures are set to 298 K for the nozzle wall and 350 K for the injector walls. Symmetry boundary conditions are used on all three symmetry planes, and the pressure is fixed at the outflow boundary of the nozzle. For the present formulation, the outflow density and three velocity components are obtained via the ghost (denoted by the subscript g) cell approach where the center of the ghost cell is located outside of the computational domain. The pressure at the outflow is fixed to a value that is less than the exit pressure of the nozzle flow.[41] Isentropic relations are used to determine density, speed of sound, and Mach number in the outflow ghost cell from the specified pressure and computed flow variables in the interior cell (denoted by the subscript i). The velocity vector at the outflow cell is then given by $\boldsymbol{V}_g = -\mathrm{M}_g a_g \hat{n} + \boldsymbol{V}_i^t$ where $\hat{n}$ is the unit normal pointing toward the interior computational domain.

For the three subsonic inflow boundary conditions, Riemann invariants are utilized. For these inflow boundaries the pressure, temperature, and inlet Mach number are specified input values. The specified conditions and computed values at the interior point are used to determine values of velocity and speed of sound for the ghost cell. More details on these boundary conditions are described in Ref. 41.

To make meaningful conclusions based on computational results, care must be taken to ensure that the differences between measured and computed mass flow rates through the injectors and primary inflow boundaries are within reasonable limits. In this study, the computed mass flow rates are strong functions of the inflow stagnation conditions.[42] These stagnation conditions are adjusted until the computed mass flow rates are in agreement with experimental values. The input values used for the laminar and turbulent computations are given in Tables 2 and 3, respectively. The difference between the experimental and computed mass flow rates (using grid D) for each of the simulations is less than 7% for each computation.[41] The experimental uncertainty in the measured mass flow rates are believed to be less than 5%.

VI. Results

A. 9257cf11: Steady-State Laminar

The initial conditions for the laminar computations were taken from the measured subsonic conditions with the Mach number = 0.01. The Reynolds number for this case based on measured subsonic conditions,[41] sonic conditions at the throat, and a throat height of 0.889 cm is 4.1×10^3. For all of the computations in this study, the Prandtl number was 0.68, and the ratio of specific heats γ was $\frac{5}{3}$. All steady-state computations were done with the temporal damping coefficients set to 0.15 and 0.05 for the inviscid and viscous terms, respectively. Second-order spatial accuracy

Table 2 Inflow values of temperature and pressure for laminar computations

Parameter	9257cf8	9257cf11
Pressures, torr		
Primary	31.67	61.54
Secondary	196.33	327.39
Temperatures, °C		
Primary	18.9	26.5
Secondary	138.0	130.0

Table 3 Inflow values of temperature and pressure used for turbulent computations of the 9257cf11 test

Parameter	Spalart–Allmaras	k–ω
Pressures, torr		
Primary	61.54	65.41
Secondary	327.39	178.74
Temperatures, °C		
Primary	26.5	26.5
Secondary	130.0	115.0

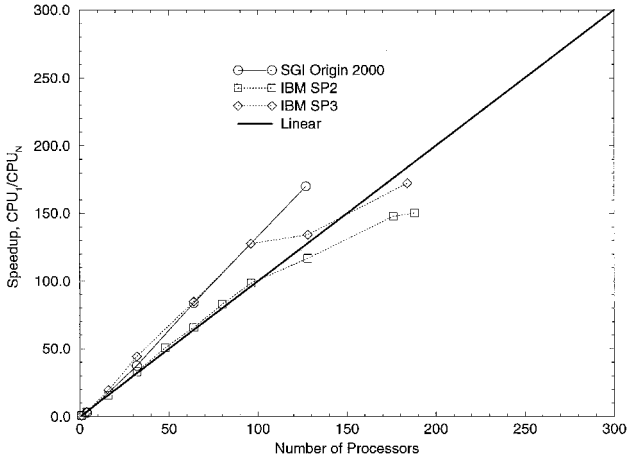

Fig. 4 Speedup results for coarse two-dimensional nozzle grid.

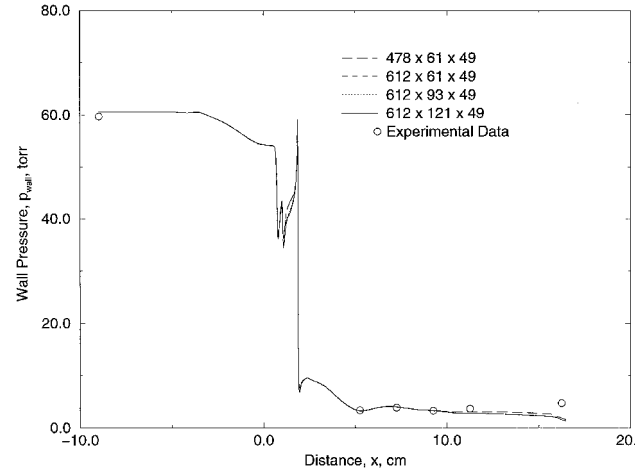

Fig. 5 Grid refinement, wall pressure for 9257cf11 experiment.

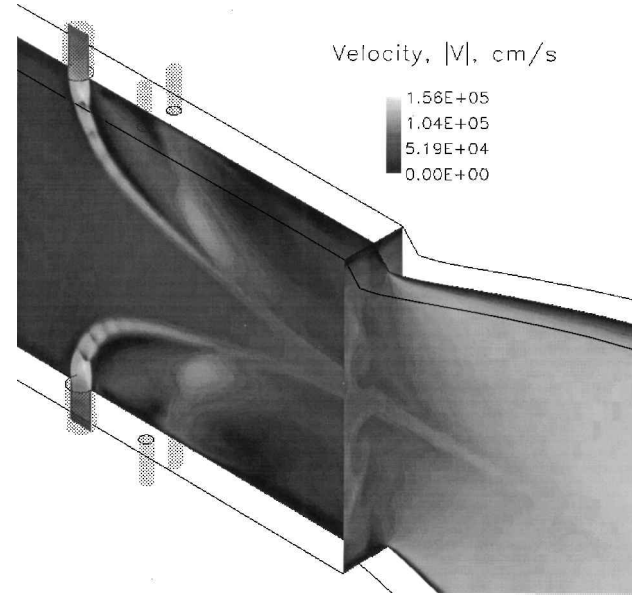

Fig. 6 Velocity magnitude contours obtained on grid *D*.

was used and 16-block Gauss–Seidel sweeps were used per Newton subiteration. A constant CFL condition was used to determine the local time step where the CFL number for each cell was set to 10^6.

The computations were considered converged when the relative change in the average y^+ value was less than 10^{-4} over 100 time steps. In this study, y^+ is defined as $\sqrt{(|\tau_w|\rho_w)}\Delta n_1/\mu_w$ where $\tau_w = \hat{n} \cdot \bar{\bar{\tau}}$. Computations performed in this study utilized three parallel computers, the IBM SP2, IBM SP3, and the SGI Origin 2000. Typical speed-up results are shown in Fig. 4 for computations performed on a coarse grid (158,000 points) similar to grid A. The speed-up results were obtained on a shared resource environment at Wright–Patterson Aeronautical System Center (ASC) using the -O3 optimization level for all compilations. The superlinear behavior has been attributed to the implementation of the block Gauss–Seidel algorithm and improved cache efficiency as the number of processors is increased.[31] The laminar results obtained on grid D were converged in 3800 steps and took 17 h on 160 processors and required approximately 75 MB of memory (per processor) with single precision on the IBM SP3.

The computed wall pressures are shown in Fig. 5 along with the measured wall pressure data. The uncertainty in the measured wall pressures is 0.5%. The agreement between the computed laminar results and the experimental data is excellent upstream of the $x = 10.0$ cm station. The small difference in pressures near the downstream end of the nozzle are believed to be due to the injection of purge flow in the z direction downstream of the nozzle throat. The effect due to the purge flow is discussed later in this section. Note that the computed temperature of the primary inflow is approximately 274 K, which compares well with the measured[41] inflow temperature of 293 K. The uncertainty in the measured temperature is less than 1%.

The velocity magnitude contours obtained using grid D are shown in Fig. 6. Note the presence of three distinct shock patterns (visible as thin dark regions) in the large injector stream. Based on the jet trajectory pattern, the current flow conditions represent a full penetration configuration where the large jet streams merge at the nozzle centerline near the throat region. The maximum height of penetration for a single transverse jet in a subsonic flow is given by the equation[43,44]:

$$y/D = 2.5(A_p/A_s)\Pi_I \tag{3}$$

For the sake of completeness, the penetration parameter based on momentum flux ratio is given by[43]:

$$\Pi = \frac{\dot{n}_s}{\dot{n}_p}\left(\frac{M_s T_s p_p}{M_p T_p p_s}\right)^{\frac{1}{2}}$$

For the current study, the value of Π_I obtained from measured subsonic conditions and estimated conditions at the point of injection was 0.16 (Ref. 41) for each of the experimental data sets. The penetration parameter determined from measured subsonic conditions Π_o, was 0.14. Because there are two secondary jet streams, the

penetration parameter used in Eq. (3) must be modified to predict the height of the large injector jet stream. In terms of cross-sectional areas, the ratio of one large injector area to one small injector is 4.0 (the computed mass flow rate ratio is actually 4.37). The measured molar flow rate for the secondary flow in Eq. (3) can, therefore, be multiplied by $\frac{2}{3}[(4 \times 230)/1380]$ to approximate the mass flow through the large injector. In addition, the pressures and temperatures used to determine the penetration height must be conditions at the point of injection. For the current configuration of the RADICL nozzle, the Mach numbers of the secondary and primary flows at the injection point are approximately 1.0 and 0.632, respectively.[41] The local conditions can be estimated using isentropic relations and the measured subsonic conditions. When all of the cross-sectional areas from the large injectors and primary nozzle geometry are used, the maximum penetration height is then given by

$$y/D = 40.725\Pi_o \tag{4}$$

This equation predicts the maximum height to be $y/D = 5.66$ for the 9257cf11 experimental data. The height obtained from the computed results is 5.5, as seen in Fig. 6, where the jets have merged at the nozzle throat. Using the modified jet penetration parameter thus provides a reasonable estimate for the maximum jet penetration height in this experiment.

The velocity magnitude contours are shown for several cross-sectional planes (at constant x) in Fig. 7. There is a complex interaction due to the large and small jet streams mixing into the primary core flow. Note that the large jet stream forms a u-shaped pattern on the second and third cross-sectional planes in Fig. 7. Because of the transverse injection of mass flows from the large and small injectors, there is a large region of low-speed flow (or separation) downstream of the injectors near the nozzle wall. As the high-speed jet streams travel downstream, viscous dissipation causes the boundaries of the jet streams to become less visible as the flow reaches the region downstream of the nozzle throat.

The surface streamlines in the injector region obtained with grid D are shown in Fig. 8. Many so-called critical points[45] are visible in this region, indicating a very complex topological structure in the region of the injectors. Note that there are two critical points upstream of the large injector. The first is a saddle point of attachment followed downstream by a nodal point of attachment. On the downstream side of the large injector there are two nodal lines of separation that extend from the large injector to terminal foci near the upstream side of the small injectors.

Velocity profiles at the throat are shown in Fig. 9. Several points of inflection due to the interaction of the jets with the primary flow

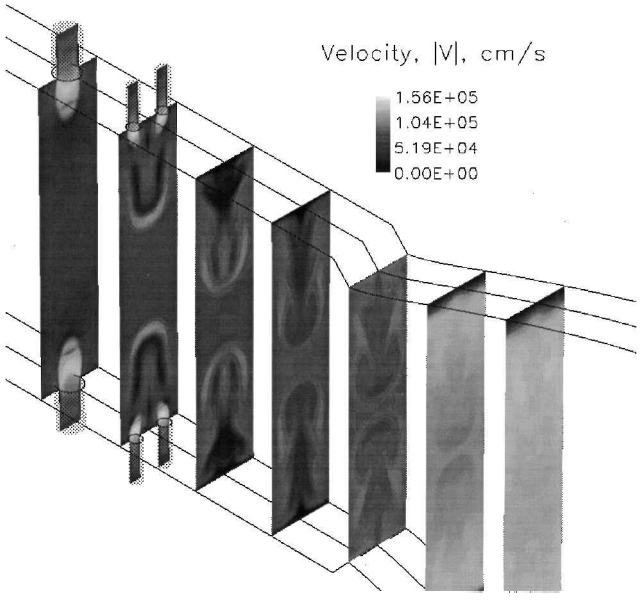

Fig. 7 Velocity magnitude contours for several planes of constant x.

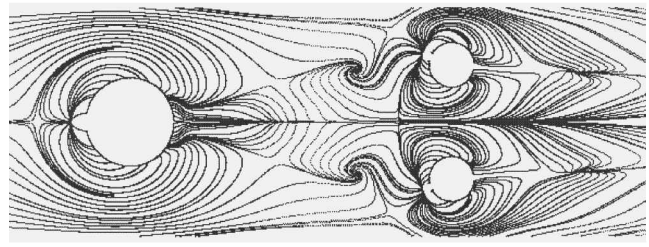

Fig. 8 Surface streamlines on nozzle wall near injectors.

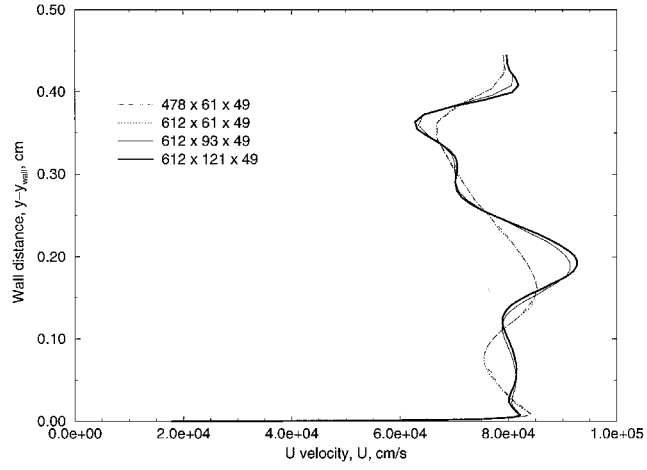

Fig. 9 Grid refinement, profiles at throat (x = 1.888 cm, z = 0.053975 cm).

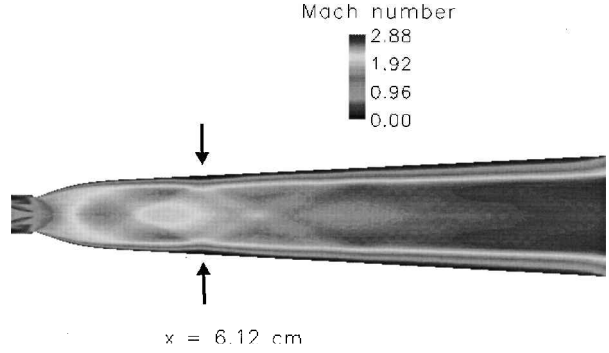

Fig. 10 Mach number contours, in nozzle region.

are visible in the profiles for grids C and D. The existence of these inflection points is often associated with unsteady phenomena.[46] This issue will be discussed later in this section. The strongest influence of the injector streams are visible in the velocity profiles at 0.40 and 0.20 cm above the wall. Mach number contours in Fig. 10 show the primary shockwave/boundary-layer interaction occurring at an x station of 6.1222 cm. The velocity profiles at this streamwise location are shown in Fig. 11. Note that streamwise separation does not occur at this location. Also note that the results obtained with grid C are very similar to the results obtained for grid D in Figs. 10 and 11.

B. 9257cf11: Time Accurate

As mentioned, the existence of several points of inflection in the profiles of velocity (as in Fig. 9) may indicate that an oscillatory flowfield exists within the COIL nozzle. This issue was investigated by utilizing the time-accurate capability of Cobalt_{60}. For these computations, second-order time accuracy was used with three Newton subiterations per time step. In addition, the value of θ was 0.95 and 48 Gauss–Seidel sweeps were used per Newton subiteration with both damping factors set to zero.[28] The time-accurate computations were performed using grid C with a starting solution consisting of a steady-state solution obtained as in the preceding section.

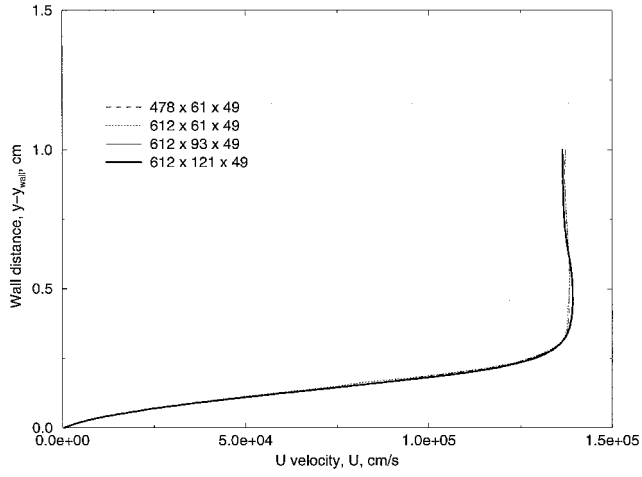

Fig. 11 Grid refinement, profiles of velocity (x = 6.1222 cm, z = 0.053975 cm).

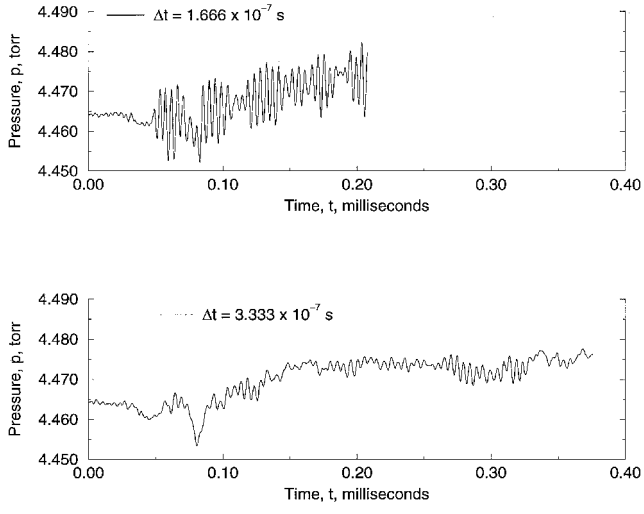

Fig. 12 Histories of pressure at x = 6.1222, y = 0.50072, and z = 0.053975 cm.

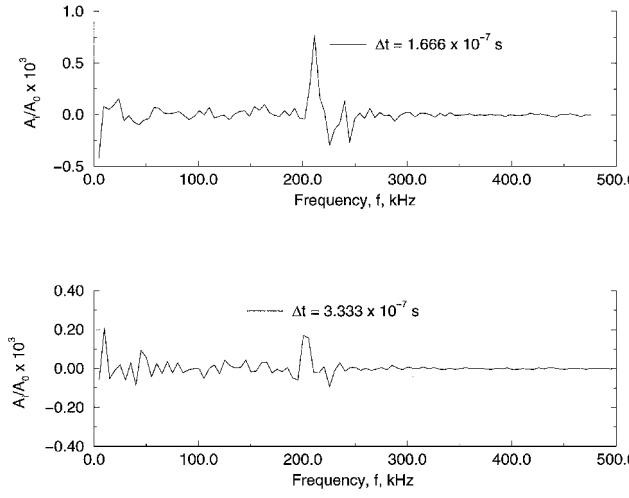

Fig. 13 Spectral coefficients of pressure time histories.

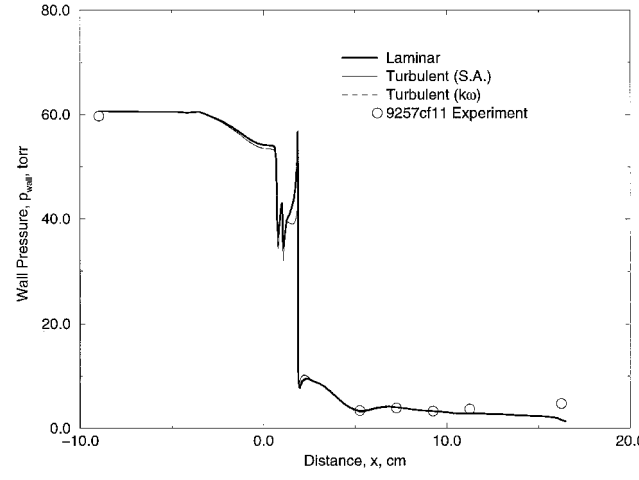

Fig. 14 Wall pressure, laminar and turbulent results for 9257cf11 experiment.

The time histories of pressures near the first shock reflection are shown in Fig. 12 for time steps of $\Delta t = 3.333 \times 10^{-7}$ s and $\Delta t = 1.666 \times 10^{-7}$ s. The maximum CFL numbers were approximately 2700 ($\Delta t = 1.666 \times 10^{-7}$ s) and 5400 ($\Delta t = 3.333 \times 10^{-7}$ s). The spectral analysis of the time history data is shown in Fig. 13. The dominant frequency for this data is approximately 210 kHz. The magnitude of velocity in this region is approximately 140,000 cm/s. From linear stability analysis of free shear layers,[47] this velocity and the dominant frequency correspond to a length scale of 0.09 cm, which is about 5% of the nozzle height at this location and about 90% of the width of the computational domain. Although not shown here, other sampling data indicate that a dominant frequency of 300 kHz occurs in the large injector region. The exit Mach number of the large injector jet stream is approximately 1.3, and the exit velocity is approximately 100,000 cm/s. A 300-kHz frequency for the large injector region thus corresponds to a Strouhal number of 0.24, which is consistent with screech tones found in ducted supersonic jets.[48] Note that the presence of three symmetry boundaries used in the computation may preclude the existence of other modes of oscillation (or instability) within the flowfield. Future study of unsteady phenomenon within the RADICL nozzle will be left for a time when the effects of chemically reacting flow can be taken into account.

C. 9257cf11: Turbulent

Two turbulence models were utilized for the 9257cf11 conditions, the Spalart–Allmaras[29] model and the k–ω model of Wilcox.[30] Computed wall pressures obtained using the finest grid (D) are shown in Fig. 14. Note that both laminar and turbulent results give nearly identical pressure distributions, with some small differences near the injector region. This observation illustrates that current experimental data are not sufficient to discern the possible existence of turbulent flow within the injector region of the RADICL nozzle.

The results obtained with the Spalart–Allmaras turbulence model were found to have a small amount of eddy viscosity near the injector region. The normalized viscosity ratio (μ_t/μ) in this region has a maximum value of approximately 12.00. Downstream of the nozzle throat, the ratio rapidly goes to zero, indicating relaminarization. Relaminarization of compressible turbulent flows with large favorable pressure gradients has been studied by many investigators.[49,50] The results obtained with the k–ω model indicate a maximum ratio of less than 4.0 in the injector region. Because of the very small amount of turbulence, the average y^+ at convergence was less than 0.15 for both computations. Results obtained on the coarsest grid (A) also indicate similar trends for the viscosity ratio. The presence of the small amount of turbulence has significant effects on the velocity profiles as shown in Fig. 15. The turbulent result obtained with the Spalart–Allmaras model has fewer inflection points, and the height of penetration of the large jet stream is visible at a lower height above the wall (approximately 0.35 cm). The reduced height of penetration (compared to the k–ω and laminar results) is due to the loss of momentum in the large injector jet stream via turbulent mixing in the injector region. The results obtained with the k–ω model are less affected because of the smaller amount of turbulent viscosity within the injector region. This demonstrates that the Spalart–Allmaras model will produce results that have

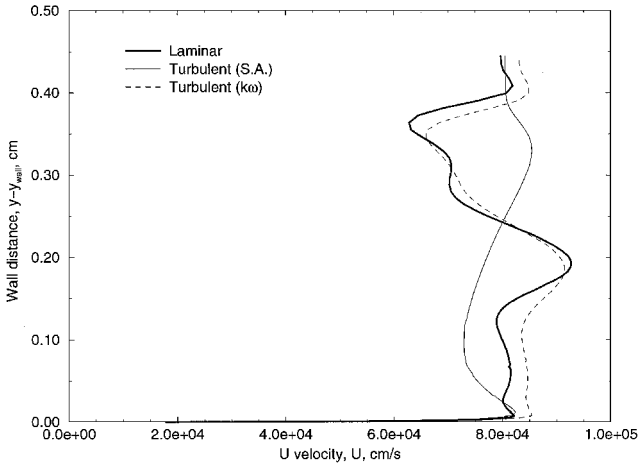

Fig. 15 *U* component profiles, throat region.

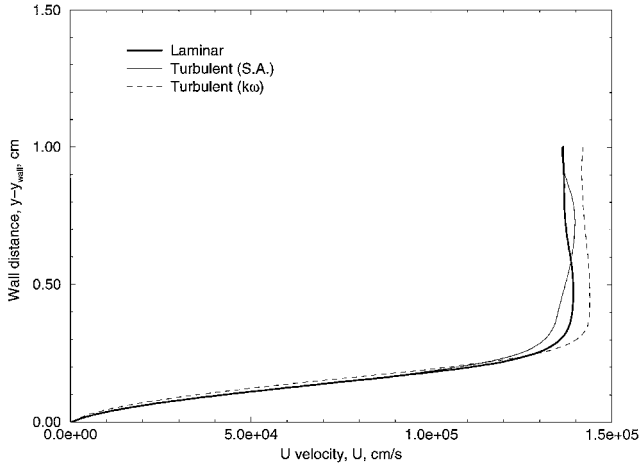

Fig. 16 *U* component profiles, shock/boundary-layer interaction region.

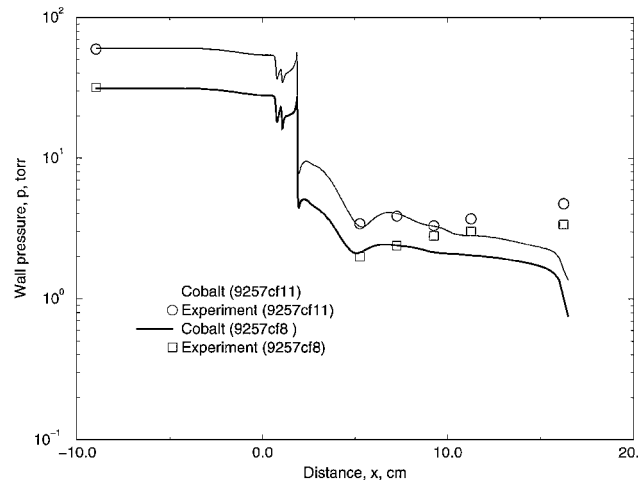

Fig. 17 Wall pressure, laminar results for both experiments.

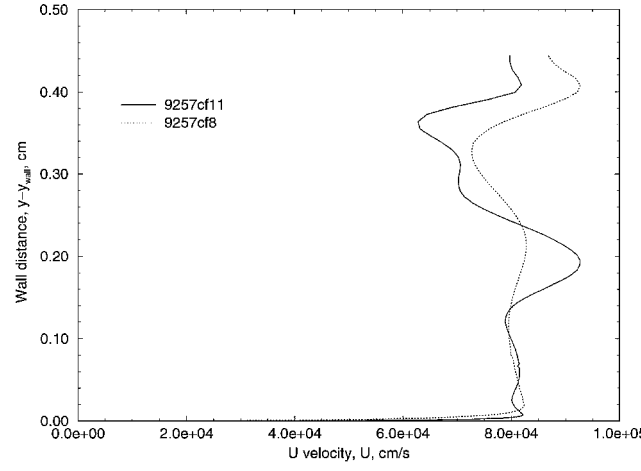

Fig. 18 *U* component profiles, throat region.

greater mixing behavior than the k–ω model for this set of flow conditions.

Based on the discussion in the preceding two paragraphs, it is clear that measured wall pressures located far from the injectors are not sufficient to determine the possible existence of turbulent flow near the injector region. However, velocity profile measurements near the injector region may be used to determine the amount and/or existence of turbulent flow within the RADICL nozzle.

The velocity profiles at the primary shock reflection in Fig. 16 show some small differences between the three computed solutions. However, the thickness of the boundary-layer for each of the computed results is essentially the same. Although not shown here, the boundary-layer thickness, heat transfer, and skin-friction coefficients downstream of the throat are nearly identical for all three computed results. This observation is consistent with the wall pressure results shown in Fig. 14.

D. 9257cf8: Laminar

The nearly identical penetration parameters permit the grids for the 9257cf11 case to be used for the 9257cf8 test case. The results obtained with grid D are grid independent for the 9257cf8 computations. The Reynolds number for this case is 2.2×10^3. Wall pressure results obtained from the laminar computations are shown in Fig. 17 for both sets of experimental data. There is excellent agreement between both sets of computational and experimental data upstream of about the $x = 9.0$ cm location. The computed inflow temperature was approximately 267 K, which agrees well with the measured temperature of 292 K. The computational results and experimental data both indicate the strong pressure rise due to the reflected shock at $x = 6.122$ cm. However, the experimental data indicate increasing pressure starting at about $x = 9.0$ cm whereas the computational results indicate a gradually decreasing pressure until the influence of the fixed outlet pressure starts at $x = 15.0$ cm.

The differences between the computational and experimental results between $x = 9.0$ and 15.0 cm are believed to be due to purge flow effects. The purge flow is added to the nozzle flow at approximately 3–5 cm downstream of the throat. The purge flow enters the nozzle region along the z direction (see Figs. 1 and 2), but then must turn 90 deg to exit the RADICL device along with the nozzle flow. The interaction between the purge flow and nozzle flow will produce a free shear layer that reduces the effective cross-sectional area of the nozzle. The growth rate of the shear layer is dependent on the differences in velocities between the purge flow and nozzle flow.[46] The flowfield properties of the purge flow near the shear layer region are difficult to determine with the existing experimental data; however, this issue will be addressed in future research efforts. Because the core nozzle flow is supersonic, the reduction in area will cause an increase in pressure. The reduction in cross-sectional area required to match the experimental data can be estimated using isentropic assumptions. Assuming an initial Mach number of 2.5 for the 9257cf11 conditions and a compression starting at 7 cm downstream of the throat, the required reduction in width z is 15%. The estimated reduction in width for the 9257cf8 conditions is also 15%. This suggests that the computational domain can be adjusted to provide a mechanism for isentropic compression so that the computational results will be in better agreement with the measured wall pressures. This will be left for future study.

Velocity profiles at the throat are shown in Fig. 18. It is clear from these results that the penetration height (at about 0.40 cm above the wall) for the 9257cf11 experiment of the large injector jet stream is identical to the height for the 9257cf8 experiment. This confirms

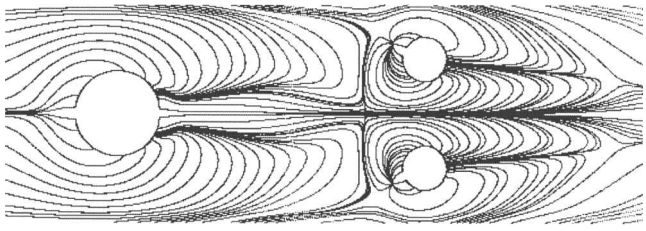

Fig. 19 Surface streamlines on nozzle wall near injectors.

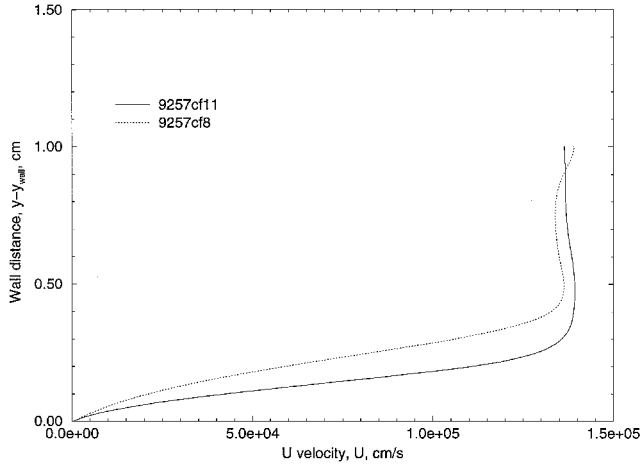

Fig. 20 *U* component profiles, shock/boundary-layer interaction region.

the similarity of the experiments in terms of the parameter Π. The influence of the small injector jet stream (at 0.20 cm above wall) is much less for the 9257cf8 experiment than the 9257cf11 test. This observation demonstrates the effects of a lower Reynolds number (while the penetration parameter is kept constant) on the jet stream interaction.

The surface streamline pattern is shown in Fig. 19. Note that several of the large-scale structures observed in the 9257cf11 case are no longer present in the current case. The lack of more complicated flow structures is due to the increased viscous dissipation present in the low Reynolds number flow. In particular, the two critical points upstream of the large injector and the saddle-foci point pair downstream of the large injector are not present in the current surface streamline pattern. The change in topology occurs through the removal or addition of saddle-nodal point pairs as predicted by critical point theory.[51]

The velocity profiles at the primary shock reflection are shown in Fig. 20 for both laminar computations. The boundary layer for the 9257cf8 (low Reynolds number) case is approximately 50% larger than the 9257cf11 (high Reynolds number) case for this x station. Although not shown here, the difference in boundary-layer thickness is of the same magnitude throughout the nozzle region downstream of the throat. Changes in the boundary-layer thickness within the nozzle region may affect predictions of extracted power in fully coupled COIL simulations because of the presence of nonuniform density regions near the nozzle wall. This will be a topic of future research efforts.

VII. Conclusions

In the present study, computational simulations have been performed with $Cobalt_{60}$ using laminar, turbulent, and time-accurate solution procedures. A grid refinement study was performed utilizing four grids. Small changes in velocity profiles were observed for the results obtained on the third and fourth grids. Experimental data from two cold-flow experiments of helium flow through the RADICL nozzle were compared with computed results. Excellent agreement between measured and computed mass flow rates were obtained for both experiments. Small differences between the measured and computed wall pressures were observed downstream of the primary shock/boundary-layer interaction. The differences in wall pressure results are believed to be due to injection of purge flow within the RADICL nozzle.

Two turbulence models indicate small amounts of numerical turbulence near the injector region, whereas relaminarization is observed downstream of the nozzle throat. The computed time-accurate results indicate dominant frequencies of 210 kHz for the experimental conditions considered. Work is currently underway to modify $Cobalt_{60}$ to simulate chemically reacting COIL flowfields, and this work will be reported in the near future.

Acknowledgments

This work was supported by the Air Force Office of Scientific Research under the direction of Robert Canfield. The computing resources were provided in part by a grant from the Department of Defense High Performance Computing Major Shared Resource Center at Wright–Patterson Air Force Base. The authors would like to thank Timothy Madden of the Directed Energy Directorate for many helpful discussions throughout this study. The authors are grateful for the assistance provided by Kenneth Wurtzler of Cobalt Solutions, LLC in generating the grids used in this study. In addition many helpful discussions with Matthew Grismer of the Air Vehicles Directorate, Charles Helms, Kip Kendrick of the Directed Energy Directorate and David Plummer of RDA Logicon are gratefully acknowledged.

References

[1]McDermott, W. E., Pchelkin, N. R., Benard, D. J., and Bousek, R. R., "An Electronic Transition Chemical Laser," *Applied Physics Letters*, Vol. 32, No. 8, 1978, pp. 469, 470.

[2]Rittenhouse, T. L., Phipps, S. P., and Helms, C. A., "Performance of a High-Efficiency 5-cm Gain Length Supersonic Chemical Oxygen–Iodine Laser," *International Journal of Quantum Electronics*, Vol. 35, No. 6, 1999, pp. 857–866.

[3]Lamberson, S. E., "Airborne Laser," *The International Society for Optical Engineering Proceedings*, Vol. 2702, Bellingham, Washington, 1996, pp. 208–213.

[4]Carroll, D. L., King, D. M., Fockler, L., Stromberg, D., Madden, T. J., Solomon, W. C., Sentman, L. H., and Fisher, C. H., "COIL for Industrial Applications," AIAA Paper 98-2992, June 1998.

[5]Carroll, D. L., and Rothenflue, J. A., "Experimental Study of Cutting Thick Aluminum and Steel With a Chemical Oxygen–Iodine Laser Using an N_2 or O_2 Gas Assist," *Journal of Laser Applications*, Vol. 9, No. 3, 1997, pp. 119–128.

[6]Yoshida, S., and Shimizu, K., " High Power Chemical Oxygen–Iodine Laser for Industrial Applications," *The International Society for Optical Engineering Proceedings*, Vol. 1225, Bellingham, Washington, 1990, pp. 478–485.

[7]Hager, G. D., Watkins, L. J., Meyer, R. K., Johnson, D. E., Bean, L. J., and Loverro, D. L., "A Supersonic Chemical Oxygen–Iodine Laser," U.S. Air Force Weapons Lab. TR 87-45, Kirtland AFB, NM, 1988.

[8]Rosenwaks, S., Furman, D., Bruins, E., and Barmashenko, B. D., "Gain Diagnostic in a Supersonic COIL with Transonic Injection of Iodine," AIAA Paper 99-3428, June 1999.

[9]Barmashenko, B. D., Furman, D., Bruins, E., and Rosenwaks, S., "Iodine Dissociation and Small Signal Gain in Supersonic COILS," AIAA Paper 99-3427, June 1999.

[10]Nikolaev, V. D., and Zagidullin, M. V., "Completely Scaleable 1-kW Class COIL with Verti-JSOG and Nitrogen Buffer Gases," AIAA Paper 99-3815, June 1999.

[11]Yang, B., Zhuang, Q., Sang, F., Chen, F., and Zhang, C., "Supersonic COIL Research Activities in Dalian, China," AIAA Paper 95-1931, June 1995.

[12]Grunewald, K., Handke, J., Entress-Fursteneck, L. V., and Schall, W. O., "Penetration Characteristics of Supersonic COIL," AIAA Paper 98-2989, June 1998.

[13]Joeckle, R., Gautier, B., Johann, N., Schellhorn, M., Sontag, A., and Stern, G., "Laser–Material Interactions with Short-Wavelength Infrared Lasers," AIAA Paper 95-1921, June 1995.

[14]Hishida, M., Azami, N., Iwamoto, K., Masuda, W., Atsuta, F. T., and Muro, M., "Flow and Optical Fields in a Supersonic Flow Chemical Oxygen–Iodine Laser," AIAA Paper 97-2391, June 1997.

[15]Masuda, W., Satoh, M., Fujii, H., and Atsuta, T., "Numerical Simulation

of a Supersonic Flow Chemical Oxygen–Iodine Laser Solving Navier–Stokes Equations," *JSME International Journal Series B*, Vol. 40, No. 1, 1997, pp. 87–92.

[16]Masuda, W., Hishida, M., and Abe, Y., "Mixing and Reacting Zone Structure in a Supersonic Mixing Chemical Oxygen–Iodine Laser with Ramp Nozzle Array," *JSME International Journal Series B*, Vol. 42, No. 3, 1999, pp. 362–368.

[17]Masuda , W., Hishida, M., and Kominato, K., "Characteristics of Radiation from a Q-Switched Supersonic Flow Chemical Oxygen–Iodine Laser," *JSME International Journal Series B*, Vol. 43, No. 1, 2000, pp. 36–45.

[18]Crowell, P. G., "Laminar Mixing Between Chemically Reacting Parallel Streams of Excited Oxygen and Iodine for an Exact Multicomponent Diffusion Model," R and D Associates Rept. 83-A/K-14-0.1984, Albuquerque, NM, 1983.

[19]Crowell, P. G., "A Vorticity-Stream Function Approach to Calculating Three-Dimensional Mixing for Viscous Parabolic Flows," R and D Associates/Logicon Rept. 87-A/K-03-02-1125, Albuquerque, NM, 1989.

[20]Crowell, P. G., and Plummer, D. N., "Simplified Chemical Oxygen Iodine Laser (COIL) System Model," *The International Society for Optical Engineering Proceedings*, Vol. 1871, Bellingham, Washington, 1993, pp. 148–180.

[21]Buggeln, R. C., Shamroth, S., Lampson, A. I., and Crowell, P. G., "Three-Dimensional Navier–Stokes Analysis of the Mixing and Power Extraction in a Supersonic Chemical Oxygen Iodine Laser (COIL) With Transverse I_2 Injection," AIAA Paper 94-2435, June 1994.

[22]Lampson, A. I., Plummer, D. N., Erkkila, J. H., Crowell, P. G., and Helms, C. A., "Chemical Oxygen Iodine Laser (COIL) Beam Quality Predictions Using Three-Dimensional Navier–Stokes (MINT) and Wave Optics (OCELOT) Codes," AIAA Paper 98-2991, June 1998.

[23]Lampson, A. I., Plummer, D. N., Crowell, P. G., and Helms, C. A., "COIL Beam Quality Predictions Using 3-D Navier–Stokes (MINT) and Wave Optics (OCELOT) Codes," *The International Society for Optical Engineering Proceedings*, Vol. 3268, Bellingham, Washington, 1998, pp. 209–217.

[24]Yang, T. T., Copeland, D. A., Bauer, A. H., Quan, V., McDermott, W. E., Cover, R. A., and Smith, D. M., "Chemical Oxygen–Iodine Laser Performance Modeling," AIAA Paper 97-2384, June 1997.

[25]Madden, T. J., and Solomon, W. C., "Detailed Comparison of a Computational Fluid Dynamic Simulation and a Laboratory Experiment for a COIL Laser," AIAA Paper 97-2387, June 1997.

[26]Madden, T. J., Carroll, D. L., and Solomon, W. C., "Investigation of High-Pressure COIL Performance Improvement Methods Using Computational Fluid Dynamics," AIAA Paper 96-2354, June 1996.

[27]Madden, T. J., Hager, G. D., Lampson, A. I., and Crowell, P. G., "Investigation of Supersonic Mixing Mechanisms for the Chemical Oxygen–Iodine Laser (COIL)," AIAA Paper 99-3429, June 1999.

[28]Strang, W. Z., Tomaro, R. F., and Grismer, M. J., "Defining Methods of $Cobalt_{60}$: A Parallel, Implicit, Unstructured Euler/Navier–Stokes Flow Solver," AIAA Paper 99-0786, Jan. 1999.

[29]Spalart, P. R., and Allmaras, S. R., "One-Equation Turbulence Model for Aerodynamic Flows," AIAA Paper 92-0439, Jan. 1992.

[30]Wilcox, D. C., *Turbulence Modeling for CFD*, DCW Indsutries, Inc., La Canada, CA, 1993, pp. 84–87.

[31]Grismer, M. J., Strang, W. Z., Tomaro, R. F., and Witzeman, F. C., "Cobalt: A Parallel, Implicit, Unstructured Euler/Navier–Stokes Solver," *Advances in Engineering Software*, Vol. 29, No. 3–6, 1998, pp. 365–373.

[32]Tomaro, R. F., Strang, W. Z., and Sankar, L. N., "Implicit Algorithm for Solving Time-Dependent Flows on Unstructured Grids," AIAA Paper 97-0333, Jan. 1997.

[33]Gottlieb, J. J., and Groth, C. P. T., "Assessment of Riemann Solvers for Unsteady One-Dimensional Inviscid Flows of Perfect Gases," *Journal of Computational Physics*, Vol. 78, No. 2, 1988, pp. 437–458.

[34]Barth, T. J., "Numerical Aspects of Computing Viscous High Reynolds Number Flows on Unstructured Meshes," AIAA Paper 91-0721, Jan. 1991.

[35]Jameson, A., and Turkel, E., "Implicit Schemes and LU Decomposition," *Mathematics of Computation*, Vol. 37, No. 156, 1991, pp. 385–397.

[36]Yoon, S., and Kwak, D., "Implicit Navier–Stokes Solver for Three-Dimensional Compressible Flows," *AIAA Journal*, Vol. 30, No. 11, 1992, pp. 2653–2659.

[37]Anderson, W. K., Thomas, J. L., and van Leer, B., "Comparison of Finite Volume Flux Vector Splittings for the Euler Equations," AIAA Paper 85-0122, Jan. 1985.

[38]Duff, I. S., Erisman, A. M., and Reid, J. K., *Direct Methods for Sparse Matrices*, Oxford Univ. Press, Oxford, England, U.K., 1986, pp. 154, 155.

[39]Karypis, G., and Kumar, V., METIS Unstructured Graph Partitioning and Sparse Matrix Ordering System Ver. 2.0, Dept. of Computer Science, Univ. of Minnesota, Minneapolis, MN, Aug. 1995.

[40]Pointwise, Inc., "GRIDGEN User Manual," Bedford, TX, 1997.

[41]Miller, J. H., Shang, J. S., Tomaro, R. F., and Strang, W. Z., "Computation of COIL Nozzle Flowfields with Transonic Injection," AIAA Paper 2000-2575, June 2000.

[42]Shapiro, A. H., *The Dynamics and Thermodynamics of Compressible Fluid Flow*, Vol. 1, Ronald Press Co., New York, 1953, pp. 82–84.

[43]Scott, J. E., Shaw, J. L. R., Truesdell, K. A., Hager, G. D., and Helms, C. A., "Design Considerations for the Chemical Oxygen–Iodine Supersonic Mixing Nozzle," AIAA Paper 94-2436, June 1994.

[44]Fearn, R., and Weston, R. P., "Vorticity Associated with a Jet in a Cross Flow," *AIAA Journal*, Vol. 12, No. 12, 1974, pp. 1666–1671.

[45]Perry, A. E., and Chong, M. S., "A Description of Eddying Motions and Flow Patterns Using Critical-Point Concepts," *Annual Review of Fluid Mechanics*, Vol. 19, 1987, pp. 125–155.

[46]Schlichting, H., *Boundary Layer Theory*, McGraw–Hill, New York, 1979, pp. 183–185.

[47]Michalke, A., "On the Inviscid Instability of the Hyperbolic-Tangent Velocity Profile," *Journal of Fluid Mechanics*, Vol. 19, 1964, pp. 543–556.

[48]Tam, C. K. W., Ahuja, K. K., Jones, R. R., III, "Screech Tones from Free and Ducted Supersonic Jets," *AIAA Journal*, Vol. 32, No. 5, 1994, pp. 917–922.

[49]Arnette, S. A., Samimy, M., and Elliott, G. S., "The Effects of Expansion on the Turbulence Structure of Compressible Boundary Layers," *Journal of Fluid Mechanics*, Vol. 367, 1998, pp. 67–105.

[50]Morkovin, M. V., "Effects of High Acceleration on a Turbulent Supersonic Shear Layer," *Proceedings, Heat Transfer and Fluid Mechanics Institute,* Los Angeles, 1955, pp. 1–11.

[51]Tobak, M., and Peake, D. J., "Topology of Three-Dimensional Separated Flows," *Annual Review of Fluid Mechanics*, Vol. 14, 1982, pp. 61–85.